PAPER

Check for updates

Development of a chromene-based fluorescent and colorimetric sensor for the sensitive detection of calcium ions in a complex medium: a detailed DFT and experimental approach

Kainat Khurshid, Kainat Gul, Hafiz Muhammad Junaid, Alam Shabbir, Umar Farooq* and Sohail Anjum Shahzad [ID] *

Calcium plays a key role in various biochemical processes and cellular functions in the human body; its imbalance can cause severe hyper- and hypo-calcemic medical conditions. In this research work, we developed a novel AIE-active chromene-based fluorescent sensor, **CFN** (DMF, λ_{exc} = 330 nm, λ_{em} = 476 nm), through an easy Knoevenagel condensation reaction with solvatochromic characteristics. The synthesized **CFN** sensor exhibited excellent fluorescence enhancement with a blue shift in 90% aqueous media (9 : 1, H_2O/DMF, λ_{exc} = 330 nm, λ_{em} = 410 nm). Blue shift in the fluorescence spectrum indicates the formation of H-aggregates, which is further supported by dynamic light scattering (DLS) results. The **CFN** sensor shows a large Stokes shift of 120 nm in pure DMF and 54 nm in water/DMF. The **CFN** sensor was employed for extremely selective and sensitive colorimetric detection of Ca^{2+} ions *via* chelation-enhanced fluorescence quenching (CHEQ) mechanism. The calculated detection and quantification limits were 10.5 nM and 35 nM, respectively. Furthermore, UV-Vis spectroscopy, fluorescence spectroscopy, and ^1H NMR titration experiments were carried out to validate the interaction mechanism between **CFN** and Ca^{2+} ions. The application of **CFN** for the detection of Ca^{2+} ions in real samples were accessed through real-time fluorescence titration analyses in human plasma, commercial milk, and different water samples. The portable **CFN** sensor-coated strips were developed for on-site sensing of Ca^{2+} ions, and a logic gate was designed to mimic it as a point-of-need calcium ion sensor.

1. Introduction

Calcium is one of the most abundant minerals in the human body, which is crucial for biological activities and human life.[1,2] It plays significant roles in body functioning, such as blood coagulation, muscle movement, metabolism, hormone secretion, fertilization, enzyme functions, gene transcription, apoptosis, and neurotransmission, which can be mainly controlled through sequential and three-dimensional variations in Ca^{2+} ions.[3] The safe calcium concentration level in blood serum is 2.12 to 2.55 mM, with 1.16 to 1.32 mM in active form, inside the human body for optimum biological functions. The concentration of calcium above this optimum level causes hypercalcemia, and below this level, it causes hypocalcemia.[4] A reduction in the albumin level in blood serum also reduces the level of Ca^{2+} ions in biological systems. Significantly low concentrations of Ca^{2+} ions are also observed in pseudo-hypoparathyroidism, malnutrition, hypoparathyroidism,

excretory system disorders, and vitamin D deficiency. Major causes of hypercalcemia include renal disorders, hyperparathyroidism, thyrotoxicosis, cancer, osteoporosis, high vitamin D intake, and sarcoidosis. The dysregulation of Ca^{2+} ion concentration in the body nerve cells is also closely related to a few neurodegenerative disorders,[5] such as Parkinson's disease (PD), Alzheimer's disease (AD), and Huntington's disease (HD).[6,7] To avoid these health risks for human beings, calcium levels in aqueous samples must be effectively monitored. Hence, procedures for the qualitative and quantitative analysis of Ca^{2+} ions in naturally and biologically occurring bodies should be accurate, less time-consuming, and economical. In this regard, innovative and high-performance sensing techniques that would allow the determination of its minimal concentration in real samples, such as food quality assessment, drinking water, human plasma analysis, medical diagnosis, and biological fluid analysis are required.

A range of techniques has been employed to determine calcium in various samples, which include titration, complexation-based spectroscopy (CBS), atomic absorption spectrometry (AAS), inductively coupled plasma mass spectrometry (ICPMS), ion selective electrode-based electrochemical

Department of Chemistry, COMSATS University Islamabad, Abbottabad Campus, University Road, Abbottabad 22060, Pakistan. E-mail: umarf@cuiatd.edu.pk; sashahzad@cuiatd.edu.pk

methods, and high-performance liquid chromatography (HPLC).[8–12] Though these approaches are quite sensitive and accurate, they require special personnel, costly instruments, and tedious sample treatment, and they suffer from the inability to perform on-spot analysis, urging the scientists to develop other methods. Thus, cost-effective, simple, sensitive techniques that can timely identify calcium on site are necessary.[13,14]

Fluorescence-based sensing techniques, being the least invasive, have shown promising results for their accuracy and applicability.[15] Calcium has been detected using many fluorescent sensors, which include calcium detection *via* mechanisms such as resonance electron transfer, chelate fluorescence, and aggregation-induced emission (AIE).[16] Some notable examples of calcium sensors are Fura-2 and Fluo-4, which have been utilized for quick and sensitive calcium detection. Certain typical organic materials show a significant aggregation-caused quenching (ACQ) phenomenon.[17] Exciplex or excimer induced by noncovalent strong interactions, such as dipole–dipole interaction and π–π stacking, results in the ACQ phenomenon. ACQ limits the practical uses of fluorophores commonly employed as solid films in real-sample analysis.[18]

Tang *et al.* (2001) discovered a phenomenon known as aggregation-induced emission (AIE), which is the opposite of ACQ.[19] AIE-active organic compounds are not capable of any emission in an organic solvent, while in a poor solvent such as water, they show enhanced emission due to aggregation. However, aggregation-induced emission (AIE) is a characteristic phenomenon observed in organic compounds in which weakly emissive fluorophores exhibit exceptional emission upon aggregation.[20,21] To induce these features, rotatable moieties are incorporated in the structure of such fluorophores *via* C–C, C–N, and N–N type single bonds.[22,23]

AIE-based fluorescence sensors enable the concurrent and localized study of calcium ions in living cells, tackling previous challenges and expanding practical applications, particularly in a complex medium. Furthermore, H aggregates typically lead to fluorescence quenching because of their high aggregation levels, which can reduce the effectiveness of fluorescence-based sensing techniques.[24] However, highly emissive H-aggregates are also reported[25,26] among which some are known to be aligned in a herringbone fashion.[27] Our designed sensor also exhibits a non-conventional photophysical behavior in its aggregated state. In this sensor, the restricted intramolecular motion and restricted intramolecular rotations contribute towards high quantum yields by enhancing radiative decay pathways despite the blue-shift caused by H-aggregates owing to the reorganization of the excited energy level to increase the energy gap. In fact, AIE originates as a result of rigidity and restriction of intramolecular motions (RIM) upon the formation of aggregates. The restriction of intramolecular motions (RIM) prevents non-radiative decay pathways and enhances luminescence. Major types of aggregates formed through self-assembly of fluorescent dyes are known as J- and H-type aggregates. These aggregates are formed based on specific types of molecular arrangements that offer distinct spectral shifts in their absorption and emission spectra compared to their monomeric

forms of fluorophores. Head-to-tail fashion arrangement of fluorophore molecules forms J-aggregates that shift the absorption and emission spectrum towards longer wavelengths compared to the monomer molecules. Sharp absorption and narrow fluorescence bands with strong intensity are characteristic features of J-aggregates. However, head-to-head (plane-to-plane or face-to-face stacking) arrangement of fluorophore molecules leads to the creation of H-aggregates. Interestingly, absorption and emission spectra of H-aggregates of fluorophores are shifted towards shorter wavelengths (blue-shift) with suppressed or no fluorescence emission properties. In H-aggregates, a shift towards a shorter wavelength in the absorption and emission spectra of the molecules is observed due to the perpendicular orientation of transition dipoles of the fluorophores.

A well-documented theory suggested the splitting of an excited electronic state into two exciton states, lower and higher energy exciton states.[28] These low- and high-energy exciton states are attributed to antiparallel and parallel dipoles, respectively. Usually, H-aggregates are characterized by observing a hypsochromic or blue shift in the absorption band owing to allowed transitions to the higher energy exciton state. A shift towards a shorter wavelength in the absorption band occurs due to forbidden transition to the lower energy exciton state with reduced transition probability. This reduced transition probability to the lower energy exciton state is responsible for the quenching of fluorescence emission in H-aggregates. However, deformation in transition dipoles allows the transitions to a lower energy exciton state, and consequently, fluorescence emission originates from the lower exciton state (Fig. 1). Interestingly, a computational study on special circumstances of H-aggregates reveals that unusual fluorescence emission occurs directly from the second exited state (S2) to the ground energy state (S0), not from the first excited singlet state (S1), as S1 is considered a dark state.[29] This kind of unusual fluorescence emission from H-aggregates is linked to an exceptional violation of Kasha's rule.

In J-aggregates, a red-shifted spectrum is obtained as a result of the allowed electronic transition from the lower-energy exciton state to the ground state. In H-aggregates, the higher-energy exciton state becomes permissible upon a co-facial/parallel arrangement of transition dipole moments of fluorophores to each other, resulting in a blue-shifted spectrum.[30] Kasha's exciton model also predicts a shift towards a shorter wavelength in the absorption spectrum of the H-aggregates as a result of forbidden transition to the lower-energy exciton states.[30,31] Generally, broad-band spectral appearance of H-aggregates is characterized with no fluorescence emission and low extinction coefficient. However, some recent studies reveal the creation of fluorescent H-aggregates and challenge the conventional understanding of H-aggregates as the only non-emissive species. For example, Modi *et al.* reported that H-aggregates of fluorinated pyridyl-azo dye exhibited a sharp absorption band with a higher extinction coefficient and demonstrated rare blue-shifted fluorescence emission in a range of organic solvents with large Stokes shift.[32] Fluorophore-like Rhodamine B is known to form highly
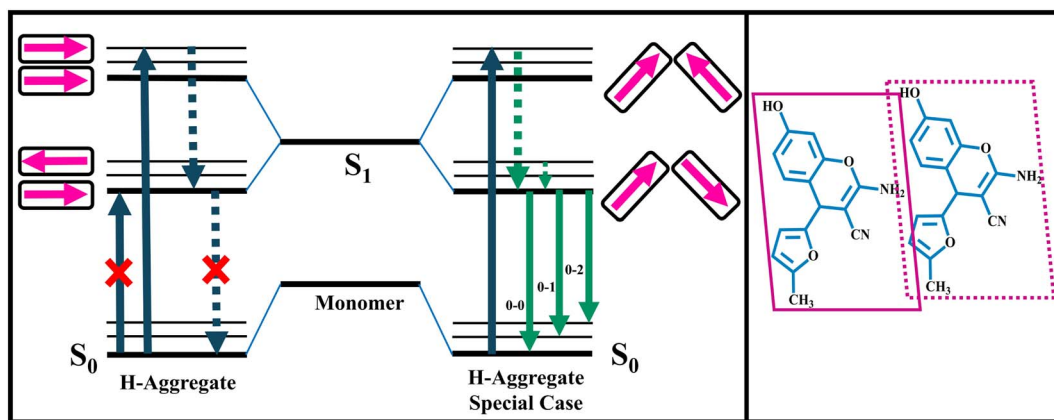
Fig. 1 Splitting of an excited electronic state into lower and higher exciton states in H-aggregates.

fluorescent H-aggregates in polar solvents.[33] Some other organic fluorophores such as Rhodamine 6G,[34] fluorescein, eosin Y,[35] cyanine derivatives,[30] thioflavin-T (ref. 36) and coumarin dyes[37] exhibited fluorescent H-aggregates. It is well known that H-aggregates are formed by plane-to-plane stacking of the molecules; however, H-aggregates of imperfectly stacked molecules offer unusual fluorescence emissions.[37–42]

In our case, with the increase in the contents of the aqueous medium, the plane of the chromene-based sensor molecules starts stacking in a twisted manner. Transition dipoles of the molecules are twisted through imperfect parallel stacking of molecules. As a result, unusual fluorescence emission occurs directly from the second exited state (S2) to the ground energy state (S0), not from the first excited singlet state (S1), as S1 is considered a dark state. As an extension of our research efforts, we aimed at developing novel fluorescent sensors.[43–46] We present the design and synthesis of a novel furan and nitrile-substituted chromene-based fluorescence sensor, **CFN**, which demonstrates aggregation-induced emission with a large blue-shift. The blue-shift in emission illustrates the formation of H-aggregates. This sensor exhibits favorable traits such as a straightforward synthesis procedure, high synthetic yield, interesting photophysical properties, and a unique molecular structure for selective sensing of calcium ions. The structural feature of the **CFN** sensor induces solvatochromic and aggregation properties. The aggregation-induced emission (AIE) character of the **CFN** sensor makes it a suitable candidate for the fabrication of solid strips, which is used for the on-site sensing of biologically important minerals. Hence, the **CFN** sensor is utilized for the selective sensing of calcium through a chelation-induced fluorescence enhancement (CHEF) mechanism. A combination of spectroscopic techniques such as fluorescence, UV-visible, DLS, and NMR titration experiments was employed to elucidate the sensing mechanism, which is responsible for selective sensing of calcium. Furthermore, all these experimental findings are supported through DFT calculations. Real-time applications of the **CFN** sensor were confirmed by experiments on real human plasma, commercial milk, and different water samples. The portable **CFN** sensor-coated strips were developed, and the logic gate was also

designed to mimic it as a worth-applying tool for the point-of-need calcium ion sensor.

2. Experimental work

2.1. Synthesis of the CFN sensor

In a well-dried and nitrogen-flushed round-bottom flask, 4.0 mmol malononitrile (0.27 g) was taken, and 5-methyl-2-furaldehyde (0.33 g, 0.3 mL), dissolved in 5 mL ethanol, was poured into it. TLC was used to monitor the course of the reaction over a seven-hour duration. Both reactants were consumed, and the intermediate was formed by the Knoevenagel condensation. With diethyl amine serving as the base and ethanol as a solvent, resorcinol (4.0 mmol, 0.45 g) was added to the intermediate. The progress of reaction was observed using TLC and refluxed for an additional 8 h. Subsequently, the crude mixture was thoroughly washed with 20 mL of distilled water and filtered. A brown residue was obtained on filter paper, which was washed again with water and dried at room temperature. Recrystallization from ethanol afforded the fluorophore **CFN**. The product was further purified by a filtration column using ethyl acetate and *n*-hexane as eluent. The desired compound **CFN** was obtained in 90% yield. ^{1}H NMR (400 MHz, DMSO-d_6): δ 9.71 (s, 1H, OH), 6.93 (d, 1H, $J = 8.4$ Hz), 6.89 (s, 2H, NH$_2$), 6.53 (dd, 2H, $J = 8.3$, 2.2 Hz), 6.38 (d, 1H, $J = 2.1$ Hz), 5.98 (d, 2H, $J = 2.9$ Hz), 4.66 (s, 1H), 2.15 (s, 3H); ^{13}C NMR (100 MHz, DMSO-d_6): δ 161.3 (C), 157.8 (C), 155.6 (C), 151.3 (C), 149.5 (C), 130.0 (1C), 120.9 (C), 112.7 (C), 111.6 (C), 106.7 (2 × C), 102.7 (C), 53.8 (C), 32.2 (C), 13.7 (C); DEPT (100 MHz, DMSO-d$_6$): δ 130.0 (C), 112.7 (C), 106.7 (2 × C), 102.7 (C), 34.2 (C), 13.7 (C).

2.2. Theoretical studies

2.2.1 DFT methodologies. DFT (density functional theory) calculations were carried out by applying the Gaussian 09 software.[47] The calculations such as geometrical optimization and electronic properties were performed at the B3LYP/6-311G(d,p) and ωB97XD/6-311G(d,p) function levels of theory. The literature has substantiated that this methodology

determines a highly accurate and precise explanation of weak van der Waals forces in contrast with other DFT functionals.[48,49] Gauss-view 5.0, Gnuplot, VMD, Gaussum, and Multiwfn 3.7 were used to analyze and visualize the output data files.[50,51] PCM (polarizable continuum solvation model) was applied to inspect the effect of solvent on electronic properties, including the density of state (DOS), frontier molecular orbital (FMO), natural bond orbital (NBO), and electron density difference (EDD), and energy of sensor and its complex with analytes.[52] NCI (non-covalent interaction) analysis was performed to evaluate the weak interactions between the sensor and the analyte. QTAIM (quantum theory of atoms in molecules) was used to evaluate the types of interactions at different BCPs (bond critical points).[53]

2.2.2 Energy optimization. Analyte–sensor interaction results in a change in energy, which was analyzed to determine the impact of the four possible contact site sensor, **CFN**. For the chosen sites, energies were calculated using eqn (1):

$$E_{int} = E_c - (E_s + E_a) \tag{1}$$

The interaction energy is represented by E_{int}, the complex energy by E_c, the sensor energy by E_s, and the analyte energy by E_a. A higher E_{int} value at a point indicates a thermodynamically stable sensor–analyte interaction. The E_{int} value, 305.04 kcal mol^{-1}, for **CFN** and Ca^{2+} present at 'site I' is most favorable for complexation.

2.3. Quantum yield calculation

The quantum yield of **CFN** and **CFN**@Ca^{2+} complex with respect to quinine sulfate ($\Phi = 0.54$, 0.1 M H$_2$SO$_4$) as a standard has been quantified using eqn (1):

$$\Phi_{CFN} = \Phi_{quinine} \times \left(\frac{I_{CFN}}{I_{quinine}} \right) \times \left(\frac{A_{quinine}}{A_{CFN}} \right) \times \left(\frac{\eta_{quinine}^2}{\eta_{CFN}^2} \right) - (1)$$

Φ_{CFN} = quantum yield of **CFN**. $\Phi_{quinine}$ = quantum yield of standard quinine sulfate. A_{CFN} = absorbance of **CFN**. $A_{quinine}$ = absorbance of standard quinine sulfate. η_{CFN} = refractive index of the sample's solvent. $\eta_{quinine}$ = refractive index of the standard's solvent (0.1 M H$_2$SO$_4$).

## 3. Results and discussion

3.1. Chemistry of CFN

The **CFN** sensor was synthesized *via* Knoevenagel condensation using commercially available 5-methyl-2-furaldehyde, diethyl amine, malononitrile, and resorcinol (Scheme 1). Initially, methyl-2-furaldehyde was treated with malononitrile to access the intermediate using Knoevenagel condensation reaction conditions. Treatment of the resulting intermediate with resorcinol using diethyl amine as a base in the presence of ethanol under reflux conditions afforded the desired fluorophore **CFN** in good yields. The progress of reaction was monitored using TLC. Recrystallization from ethanol afforded the fluorophore **CFN** in 90% yield.

NMR spectroscopy was used to characterize the structure of the synthesized product **CFN**. The ^{1}H NMR spectrum of the **CFN** sensor shows a characteristic signal at δ 9.71, corresponding to the hydroxyl (OH) proton, the multiplet in the range of 5.99 to 5.93 ppm and the singlet at 2.16 ppm are assigned to the furan ring protons and methyl group, respectively, confirming the incorporation of the 5-methylfuran-2-yl moiety into the chromene framework. Additionally, the ^{13}C NMR spectrum exhibited fifteen peaks that are attributed to fifteen unique carbon atoms of the synthesized compound. Seven peaks that appeared in the DEPT135 NMR spectrum demonstrate the presence of hydrogen-attached carbon atoms that confirmed the formation of desired compound **CFN**. The details about the procedure, instruments, titration experiments, and reagents are provided in the SI (SI-1). The SI also contains the characterization data (S25–S42).

3.2. Comparison with previous sensors

Calcium ion sensing has been a topic of research for many years, which leads to a great collection of scientific results in this domain. Despite all the great contributions of previous research, there is always room for improvement, and great work done previously acts as a steppingstone for those improvements. **CFN** is a new effort for improvement in the field of fluorescent sensors. Calcium ion sensors developed earlier are mentioned in Table S1, which depict the type of studies performed and parameters mentioned. Many of those sensors have a better LOD than **CFN**; however, some lack ease of synthesis to access fluorophore, pH studies, real sample tests, binding efficiency record and underlying mechanism discussion. Among all the sensors mentioned, Ankireddy *et al.* developed a most efficient Ca^{2+} sensor with all its excellent properties; however, it is a quenching-based sensor leaving the room for noise or false positivity.[54] Some sensors were organelle specific and were not tested in water and milk samples such as that developed by Hong *et al.*, Shen *et al.*, Zhang *et al.*, Cao *et al.*, and Gomes
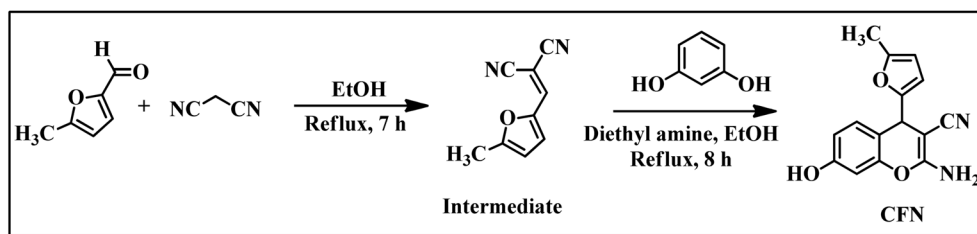
Scheme 1 Synthetic protocol to afford the desired fluorophore **CFN**.

et al.[55–59] Some other sensors either have a specific pH range for calcium ion detection needs and an extra step of buffer addition such as in the case of Hong *et al.* and Kacmaz *et al.*[55,60] Some of the mentioned sensors are not fully selective such as that by Gomes *et al.* and Cao *et al.*[58,59] In comparison to all these **CFN** sensor is an easy to synthesize, highly selective, super sensitive sensor applicable in a wide range of pH, temperature and type of samples.

3.3. Photophysical properties based on structure–property relationships

3.3.1 Optical intensity optimization. Organic fluorophores typically exhibit a diverse emission behavior in solvents with different polarities and concentrations due to extended π-conjugations. Considering these properties, fluorescence analysis of **CFN** ($\lambda_{\text{excitation}} = 330$ nm, $S_w = 3/3$) was carried out at concentrations ranging from 10 μM to 100 μM. It showed the best emission at 30 μM (Fig. S1). The fluorescence emission

intensity at 10 μM and 20 μM is much lower; therefore, 30 μM is considered as the optimal concentration for further studies. Notably, significant quenching in fluorescence response was observed at concentrations above 30 μM. The diminished emission intensity at increased fluorophore concentrations is attributed to the inner filter effect, where the emission energy of the inner layers is reabsorbed by the outer layer of molecules.[61] It was found that 30 μM is the optimized concentration of **CFN** ($\lambda_{\text{excitation}} = 330$ nm, $S_w = 3/3$, $\lambda_{\text{emission}} = 476$ nm) with a quantum yield $\Phi = 0.175$, where the **CFN** sensor exhibits maximum emission with minimum primary inner filter effects. At 30 μM concentration, **CFN** exhibits a minimum inner filter effect (IFE) and a large Stokes shift of 120 nm, which nullifies secondary IFE (Fig. S2a).

3.3.2 Solvatochromism. The structural features of **CFN** motivate us to investigate the optical emission properties of **CFN** in different organic solvents. The optimized 30 μM concentration of the **CFN** was scanned in solvents of varying polarity, such as acetone (ACT), EtOAc, ACN, MeOH, DMF,
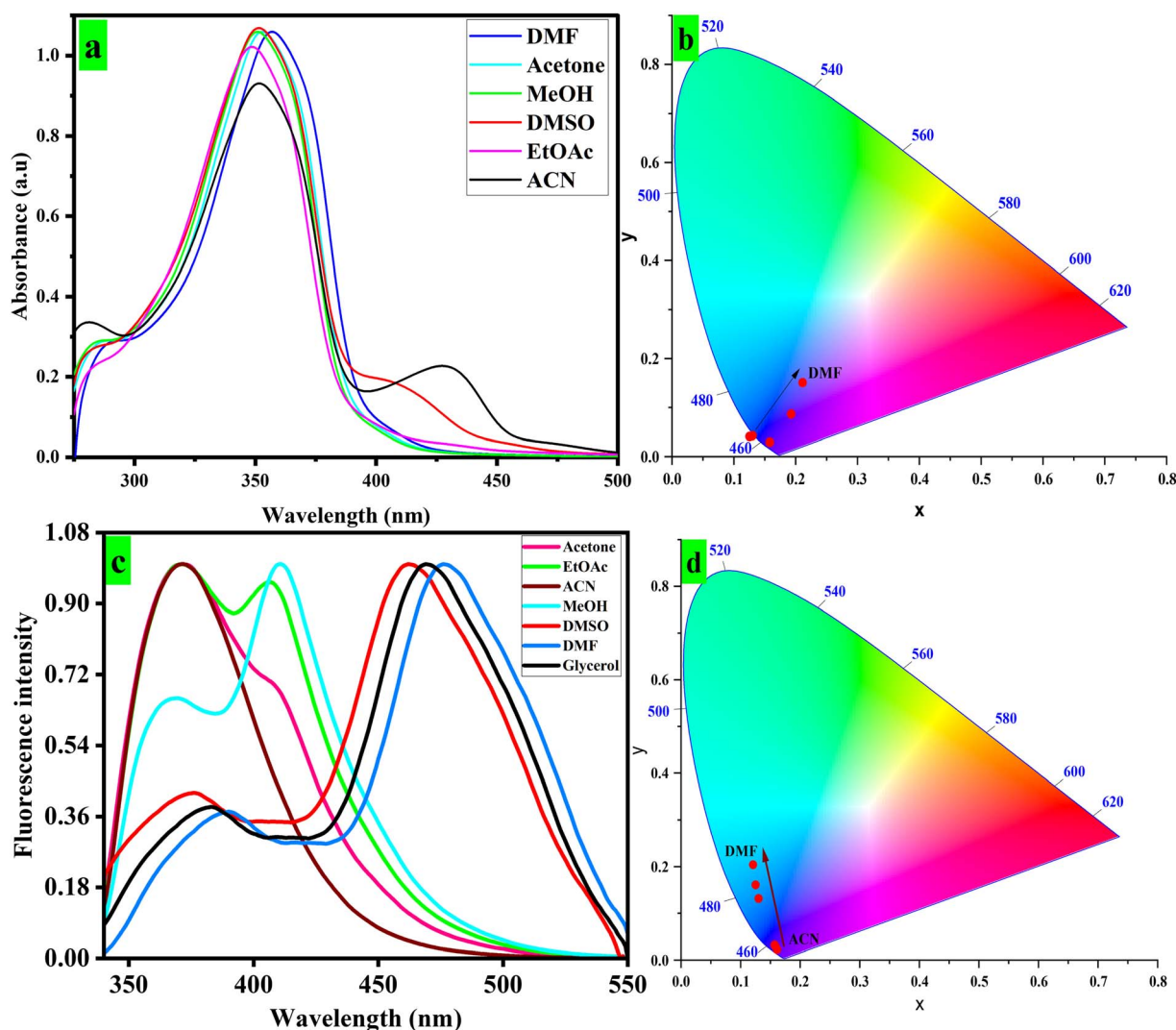

Fig. 2 Absorption spectra of fluorophore **CFN** in different solvents (a), CIE diagram for absorption spectra (b), emission spectra of fluorophore **CFN** (c), and CIE diagram for emission spectra (d).

DMSO, and glycerol (Fig. 2). The **CFN** fluorophore exhibits n–π* and π–π* transitions, which are responsible for the appearance of absorption bands at different wavelengths depending on the types of dominance of the possible transition. Fluorophore **CFN** exhibits a maximum absorption band at 348 nm in ethyl acetate. A significant red shift was observed in DMF (356 nm), illustrating stabilization of the excited state of the **CFN** fluorophore in a polar aprotic solvent, probably due to high dielectric constant, viscosity, interaction with the fluorophore, and good lone pair donating ability. Acetone (352.5 nm), ACN (352 nm), and DMSO (352 nm) show almost similar absorption bands, indicating the same polarity effect (Fig. 2a). Polar solvents interact with π* electrons through dipole–dipole interaction and stabilize the excited state more significantly than the ground state, resulting in a bathochromic shift. DMSO is an aprotic but highly polar solvent that stabilizes polar compounds. **CFN** becomes more polar in its excited state, and DMSO stabilizes its excited polar state with reduction in its energy gap, leading to a substantial red shift as compared to less polar solvents. While in the case of methanol, n–π* transition forms hydrogen bonding with a fluorophore and stabilizes its ground state, which increases the energy gap between ground and excited states (n–π*), resulting in a slight blue shift. The chromaticity diagram demonstrates the overall variation in absorption wavelengths in different solvents (Fig. 2b).

Similarly, the **CFN** exhibits maximum emission at different wavelengths in different polarity solvents such as ACN (370 nm), acetone (373 nm), EtOAc (409 nm), MeOH (410 nm), DMSO (462 nm), glycerol (469 nm) and DMF (476 nm) depending on solvent viscosity, their interactions with the **CFN** fluorophore and their respective dielectric constants (Fig. 2c). Moreover, the CIE diagram illustrates the changes in emission wavelengths (Fig. 2d). The ground- and excited-state emissions of fluorophores are impacted by solvent polarity, resulting in a change in absorption and emission properties.[62] Additionally, the free-rotating phenyl rings attached to the developed sensors impart various optical properties in response to changes in the solvent polarity. The study of Stokes shift, dipole moments and charge translations such as twisted intramolecular charge transfer (TICT) and intermolecular charge transfer (ICT) in sensor molecules is made possible by solvatochromism.[63] As shown in Fig. 2, **CFN** displayed a red-shift in absorption bands within the range of 348 nm to 356 nm with the increase in solvent polarity. The π–π* transition attributed to the bathochromic shift of 8 nm for **CFN** was observed in absorption spectra when moving from low- to high-polarity solvents. As evident from the emission spectrum, the more proclaimed positive solvatochromic behavior is probably due to extended π conjugation in the molecular structure. The **CFN** sensor displayed intense emission bands at 476 nm in DMF. Furthermore, a 106 nm bathochromic shift was observed when moving from low- to high-polarity solvents. For example, emission of **CFN** is observed at 370 nm in acetone compared to 476 nm emission maxima in DMF.

Generally, under high polar conditions, fluorophores encounter solvent relaxation, resulting in longer wavelength emissions due to vibrational energy at the excited state being transferred to surrounding molecules.[62] The notable changes in fluorescence intensity and wavelength (λ_{max}) are also observed due to the impact of polar solvents on dipole moments of excited fluorophores.[64] The photophysical properties of the sensors that have been developed are summarized in Table S2. The quantification of emission changes for the sensor due to solvent polarity was further done using the Lippert–Mataga plot, which displayed linear relationships ($R^2 = 0.795$) between Stokes shifts and polarizability (Δf) (Fig. S3a).[65] These plots were further considered to investigate solvatochromism *via* the change in dipole moments ($\Delta\mu$) among the excited and ground states, which gave 9.7 D for **CFN**. The dipole moment ($\Delta\mu$) values infer that the developed sensor can discriminate between solvents of varying polarity. The detailed structure–property relationship studies prompted the application of the developed material for biological and environmentally crucial metal ions. Further optical studies were carried out in DMF due to the substantial quantum yield and Stokes shift in fluorescence emission observed.

3.3.3 Optical studies based on aggregation-induced emission (AIE).

Present twisted substitutes on organic fluorophores result in negligible fluorescence emission in dilute solutions, but the optical response is enhanced by aggregation or formation of solids, the process termed AIE.[20,66] AIE was incorporated into the **CFN** core by adding freely rotatable phenyl rings *via* –C–C– association. The optical characteristics of the sensor were examined by gradual addition of water (0–90%) in DMF. The sensor was found to be sparingly soluble in a water–DMF combination but thoroughly soluble in organic solvents. Hence, the DMF : H_2O mixture was chosen for aggregation studies. However, with a further change in water contents (20–80%), a significant increase in absorption was observed for **CFN** with a steep increase in absorbance from 80% to 90% water fraction (Fig. 3a). Further addition of water did not change the absorption spectra, and the Mie scattering effect characterized by a level-off tail was noted (Fig. 3a). The absorption bands are changed slightly with water fractions (0–90%) in DMF due to the solvent polarity effect, and the overall linear response of the **CFN** sensor was observed with the increase in water fraction (Fig. 3b).[67]

Various amounts of water (f_w = 0–90%) were added to the DMF solution of the sensor to conduct thorough emission experiments. Despite extended π-conjugation, **CFN** showed comparatively weak emissions in DMF caused by non-radiative decay routes of free rotation of phenyl rings. However, with the addition of water, the emission intensity of **CFN** (30 μM) significantly increased by shifting from 476 nm to 410 nm (Fig. 4a). These absorption changes with increased water proportions suggest the H-aggregate formation.[68] Moreover, with the increase in water fractions (0–90%) the emission enhancement of about 5 times for **CFN** was seen with a blue-shift of 66 nm, further indicating the formation of H-aggregates.

The quantum yield of **CFN** also increased from $\Phi = 0.175$ to $\Phi = 0.420$. The **CFN** shows a Stokes shift of 54 nm at 90% water fraction (Fig. S2b). The higher water content results in the formation of well-organized aggregates. The aggregate formation was characterized through the monitoring of particle size
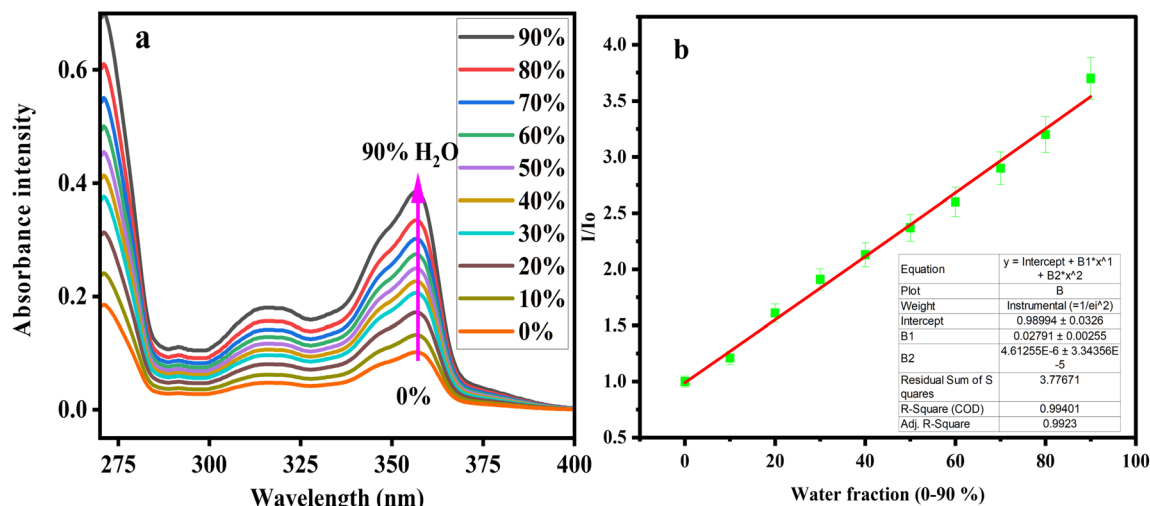
Fig. 3 UV-Vis absorption spectra (a) and linear-fitting regression line (b) calculated after gradual mixing of water fractions (0–90%) in a 30 μM DMF solution of the **CFN** sensor.
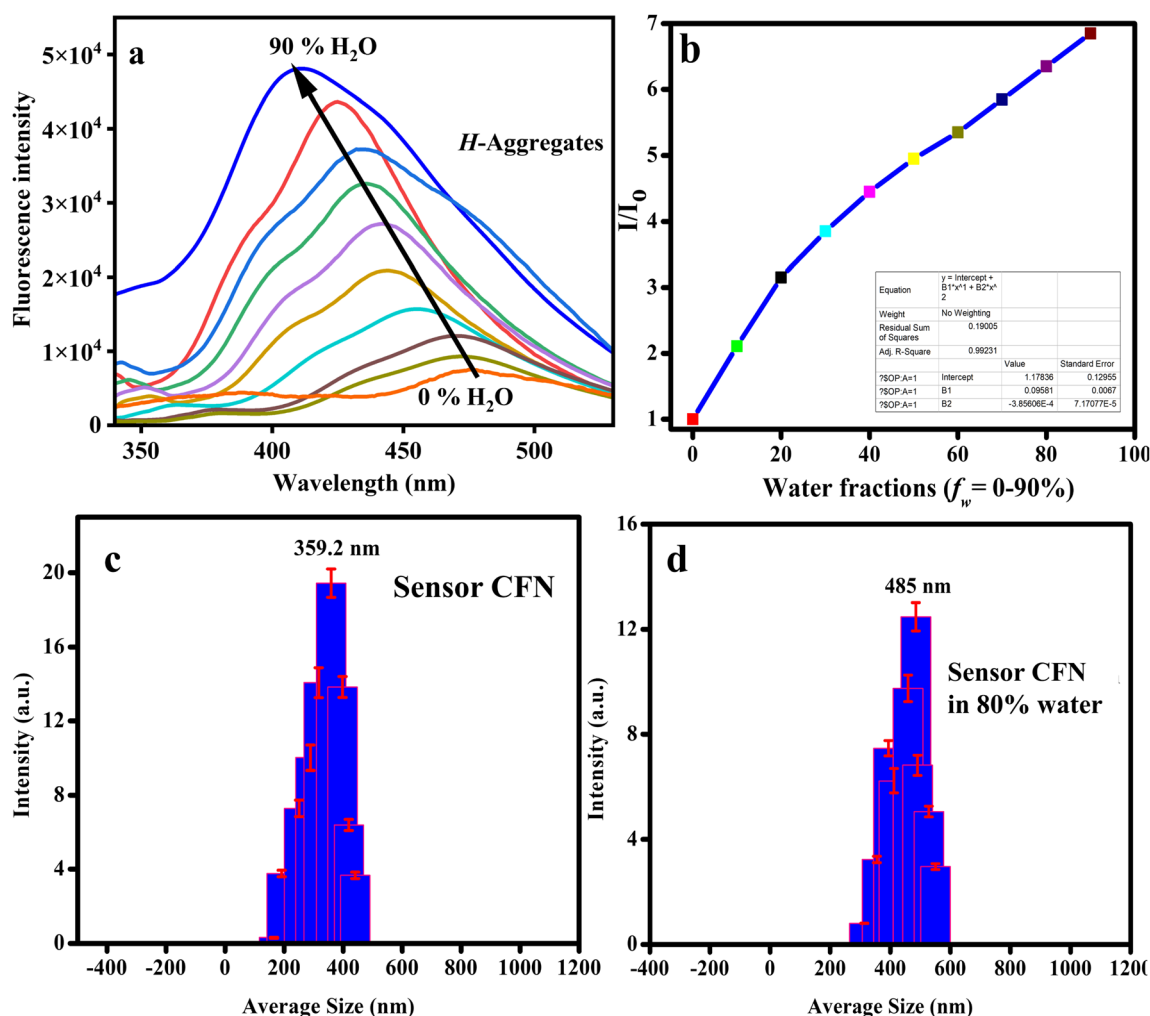

Fig. 4 Fluorescence spectra of the **CFN** sensor (30 μM) at consistently increasing water fractions (f_w = 0–90%) in aqueous solutions (a) and a polynomial fit plot demonstrating the association between emission intensity and different water contents (b). DLS size distribution analysis of the **CFN** sensor (c) and after the addition of 80% (d) water portion into its 30 μM DMF solution.

via dynamic light scattering (DLS) analysis (Fig. S3b). The particle size kept increasing from 359 nm to 485 nm upon increasing the water content from 0% to 80% (Fig. 4c and d). The free rotations of substituted phenyl rings (RIR) in the molecules are also suppressed, resulting in non-radiative decay pathways and enhanced fluorescence.[69]

Using a polynomial fit plot, the determination of the correlation between emission intensity and the addition of water fraction in DMF solvent was made possible (Fig. 4b). The materials showing enhanced fluorescence through the AIE mechanism ought to exhibit consistent behavior in a viscous environment.[70]

3.4. Photosensitive detection of biologically important nutrient calcium

The **CFN** sensor (H_2O : DMF, 9 : 1, v/v, 30 μM), with $\lambda_{exc} = 330$ nm, $S_w = 3/3$, and $\lambda_{emission} = 410$ nm, possesses unique structural features with nitrogen heteroatoms, which uniquely show complexation with metal ions. This characteristic prompted us to evaluate the detection capabilities of the sensor against various metal ions in various media, including food, water, and industrial effluents. We tested the specific concentrations (1000 nM) of a range of metal cations with competing anions including Cu^{2+}, Cr^{3+}, $Fe^{3+/2+}$, Mn^{2+}, Mg^{2+}, Al^{2+}, Zn^{2+}, Ni^{3+}, Ca^{2+}, Co^{2+}, Ag^+, Na^+, Pb^{2+}, K^+, Hg^{2+}, Ba^{2+}, SCN^-, I^-, F^-, Cl^-, Br^-, SO_4^{2-}, NO_2^-, CN^-, HSO_3^-, OAc^-, OH^-, NO_3^{2-}, HS^-, and BrO^- with an AIE-active **CFN** sensor. The emission spectra were obtained in H_2O : DMF (9 : 1, v/v, 30 μM, $\lambda_{excitation} = 330$ nm, $S_w = 3/3$), as shown in Fig. 5.

The **CFN** sensor displayed an intense peak at 410 nm upon the addition of a wide range of metal ions. However, a significant quenching of fluorescence emission was observed at 444 nm for Ca^{2+} (500 nM). This indicates distinct and preferential complexation of the sensors with calcium ions. Additionally, a noticeable change in color from pale yellow to dark yellow with the addition of 1 μM calcium further indicated the utility of the developed sensor for naked-eye detection of the analyte in daylight (Fig. S4).

Given the identical absorption and color changes of the AIE-based **CFN** sensor for the oxidation state (Ca^{2+}). Ca^{2+}-focused UV-visible absorption experiments were conducted by analyzing the change in the absorption spectrum of **CFN** by gradually increasing the amount of Ca^{2+} (0–1000 nM) (Fig. 6). As shown in Fig. 6, the intensity of the absorption peaks of **CFN** at 356 nm was progressively increased. A substantial change in the color of **CFN** was observed after the addition of Ca^{2+} ions under a UV 365 nm lamp (inset Fig. 6b). The absorption intensity reached its maximum concentration (1000 nM) in a solution containing H_2O : DMF (9 : 1 v/v), indicating stronger analyte-sensor complexation. Further fluorescence emission experiments were conducted to investigate the sensitivity of the AIE-based **CFN** sensor to calcium after the absorption studies. The emission spectra of the sensor were taken before and after complexation with the analyte (Fig. 7). With the increase in Ca^{2+} concentration, the fluorescence emission of **CFN** steadily decreased starting from 410 nm emission maxima and achieving the highest quenching at 1000 nM at 444 nm emission maxima, leading to a bathochromic shift of 34 nm (Fig. 7). The quantum yield of **CFN** decreased from $\Phi = 0.420$ to $\Phi = 0.035$.

The sensitivity of the AIE fluorescence-based **CFN** sensor was confirmed by calculating the limit of detection (LOD) using the established IUPAC procedure.

The LOD of 10.5 nM with **CFN** was found against Ca^{2+}, which is significantly lower than the permissible calcium level of 2.12–2.62 mmol L^{-1} by WHO recommendations in dietary supplements and previously reported literature (Table S2).[71]

The results align with the absorption experiments, supporting the **CFN**–Ca^{2+} complex, which is supported by atomic
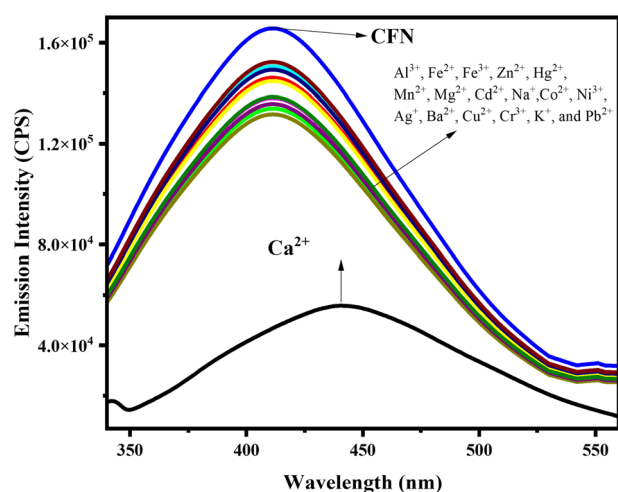

Fig. 5 Fluorescence emission spectra of the **CFN** sensor scanned in the presence of a range of competing metal ions. The emission spectra were obtained in H_2O : DMF (9 : 1, v/v; 30 μM; $\lambda_{exc} = 330$ nm; $S_w = 3/3$).
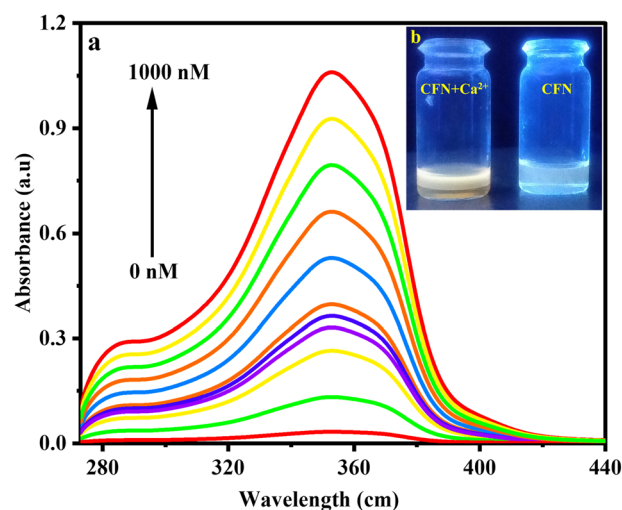

Fig. 6 UV-Vis absorption spectra generated after the concomitant addition of Ca^{2+} (0–1000 nM) to aqueous solution (water : DMF = 9 : 1, v/v) of the **CFN** sensor (a) and photographs showing the visual colorimetric detection of Ca^{2+} under a 365 nm UV lamp (b).
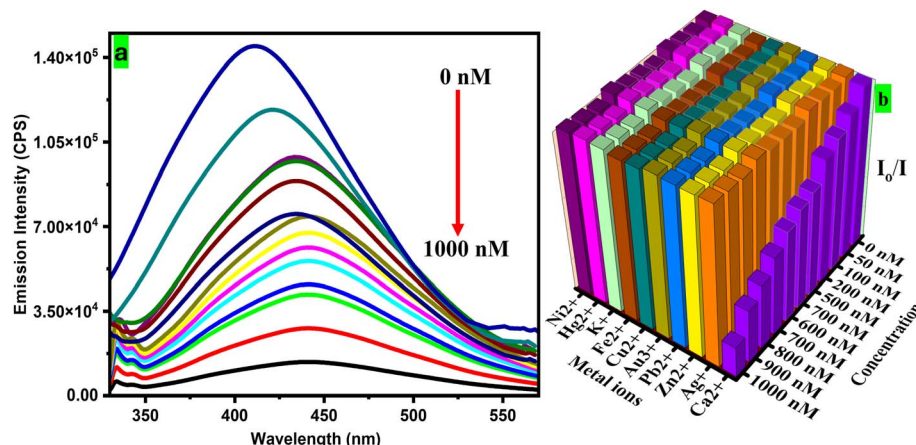
Fig. 7 Fluorescence emission spectra (a) and the corresponding 3D Stern–Volmer plot (b) of the **CFN** sensor upon the consistent addition of Ca^{2+} (0–1000 nM) in aqueous solutions ($H_2O : DMF = 9 : 1$, v/v).

radius, charges, and binding energy of calcium metal ion. In Fig. 7b, 3D SV plot demonstrates a selective quenching against Ca^{2+} ion. A linear relationship between the fluorescence intensity and the analyte concentration was found by calculation using the Stern–Volmer plot. With a significant correlation coefficient value of 0.999, it suggests a single chelation-enhanced quenching mechanism for **CFN** (Fig. S5). The SV binding constants (K_{sv}), value for Ca^{2+} were determined to be 1.76×10^{-7} M^{-1} with **CFN** (Fig. S5). Additionally, **CFN** exhibited stable emission upon exposure to 100 equivalents of interfering species, thus showing good selectivity towards the Ca^{2+} analyte (Fig. S6). The sensitivity of the developed sensor was further implied by the continuous variation method, and the output was plotted to elucidate its binding stoichiometry. The solvent system $H_2O : DMF$ (9 : 1, v/v) with a fixed concentration of **CFN** was utilized to analyze various mole fractions (0–1.0) of the analyte. The results suggested a 1 : 1 complexation stoichiometry between metal ions and the developed highly selective AIE sensor (Fig. S7). The fluorescence results were corroborated by density functional theory (DFT) studies (*vide infra*). Hence, after thorough UV-visible absorption and fluorescence emission experiments, the **CFN** sensor was found to be a suitable choice for sensitive and selective monitoring of Ca^{2+} in aqueous media ($H_2O : DMF$).

3.5. Analysis of counter ions and reversibility

The specific chelation of Ca^{2+} with **CFN** was further examined through counter-experiments. Aqueous solutions of various calcium salts, including $CaSO_4$, $CaCl_2$, CaF_2, and CaI_2 were added to the sensor solution, followed by emission analysis (Fig. S8). The results established the selectivity of **CFN** even in the presence of counter ions. In addition, reversibility is an important parameter of a sensor for the development of real-sample analysis. The reversible detection of calcium was achieved by the addition of ethylene diamine tetraacetic acid (EDTA, 0–3 equivalents) to a metal-sensor complex (1 μM Ca^{2+}) in an optimized solvent medium (9 : 1, $H_2O : DMF$) (Fig. S9). The

original fluorescence intensity was restored outstandingly, thus successful release of calcium from the complex was confirmed.

3.6. Evaluation of pH, photostability and response time

For ensured real-time application of **CFN**, its behavior under various pH conditions and photostability was assessed. The emission response of **CFN** (10 μM) was taken across a pH range of 1–14 (Fig. S10). Significant quenching in response to the presence of the analyte was observed over the pH range (5.0–11.0), indicating the suitability of the observed pH range for Ca^{2+} sensing (Fig. S11). Sensor response time was evaluated for real-time applicability of the sensor. The sensor was mixed with a 500 nM Ca^{2+} solution, and a fluorescence change was monitored over 0–60 seconds time periods. Significant quenching after 10 seconds was observed for **CFN** up to 60 seconds (Fig. S12a). Similarly, the quenching response of **CFN** was tested under different temperatures from 28 °C to 38 °C, and the results remained promising as evident from Fig. S12b. These findings demonstrated the potential of the sensor as a reliable tool for the sensitive, selective, and rapid on-site detection of Ca^{2+} in aqueous media.

Another vital aspect of practical applications of fluorescence-based sensors is its photostability. Following exposure to high energy excitation radiation, the emission of the sensor was observed, in both the presence and the absence of analytes in a selected $H_2O : DMF$ solvent combination (Fig. S13). The promising stability of the developed sensor was confirmed under the tentative conditions by no disruption in emission and sensing response.

3.7. Mechanism of the CFN sensor for Ca^{2+} detection

3.7.1 Possible mechanism of sensing. The distinctive characteristics based on the structure of the AIE-active **CFN** sensor make it more selective for Ca^{2+}. The nitrogen atom of the nitrile group, oxygen from the furan ring, and protons of the methyl group interact with Ca^{2+}, even in the presence of interfering species. Calcium and magnesium are known to undergo

chelation with compounds or ligands *via* nitrogen and oxygen.[72] Doubtlessly, the –OH group in the structure of **CFN** can potentially interact with the calcium ion. In this regard, the calcium interaction with the –OH group must exhibit a blue-shift in the emission spectra of the **CFN** sensor due to reduced intermolecular charge transfer from the phenolic OH group to the other end of the molecule, where the electron-withdrawing cyano group and oxygen of furan ring are present in the **CFN**@Ca^{2+} complex. This reduced flow of intermolecular charge transfer (ICT) can significantly reduce the electronic conjugation and charge separation. Subsequently, reduced conjugation and charge separation should result in a blue-shift with decreased fluorescence emission that is not observed in the emission spectra of **CFN**. In contrast, nearly a 34 nm bathochromic shift was noticed in the emission spectra of **CFN** after its interaction with calcium ions that ruled out the possible interaction of calcium ions with the –OH group. The absence of ICT with a blue-shift clearly demonstrates that the interaction of calcium with the –OH group is negligible or its complexation with the –OH group is not stable enough. Furthermore, DFT calculations were performed multiple times and every time DFT did not support the interaction of calcium ions with a phenolic hydroxyl group. Probably, the calcium ion has been trapped by the other side of the molecule functional groups instead of the hydroxyl moiety through the presence of combined significant interaction of nitrogen of the cyano group and oxygen of the furan ring system with calcium ions in **CFN**. Due to this, calcium forms a stable complex with the nitrile group, the oxygen of furan and the hydrogen of methyl group in **CFN** that is validated through computational analysis. The dynamic light scattering (DLS) technique authenticated the chelate formation more significantly. The particle size monitored upon water

aggregation (485 nm) increased immensely after the formation of **CFN** with calcium ions to 890.2 nm as shown in Fig. S14. The AIE-active fluorescent **CFN** sensor exhibits emission intensity in DMF/water due to the minimum inner filter effect and absence of intramolecular charge transfer, when the **CFN** interacts with Ca^{2+} and starts chelation (**CFN**@Ca^{2+}). After chelation, the **CFN**@Ca^{2+} complex is formed in which the binding of Ca^{2+} ions facilitates the intramolecular charge transfer in the **CFN** molecule. Therefore, the ICT changes the overall electronic environment of **CFN**, which directly induces the non-radiative decay and quenches the emission intensity of the **CFN** sensor. This phenomenon is also known as chelation-quenched fluorescence (CHEQ). The CHEQ is the main sensing mechanism involved in the sensitive and selective sensing of Ca^{2+} ions. Moreover, the interaction between **CFN** and Ca^{2+} ions was further validated through DFT calculations. FMO and DOS analysis demonstrate the significant reduction in HOMO–LUMO energy gap that validates the sensitivity of **CFN** toward Ca^{2+}. Additionally, EDD analysis represents the distribution of charge over the **CFN**@Ca^{2+} complex and 2D, 3D-NCl analysis demonstrates the types of interactions present between **CFN** and Ca^{2+} ions. Furthermore, QTAIM analysis illustrates the chelation between **CFN** and Ca^{2+} ions.

Job's plot was drawn based on fluorescence titration experiments at different mole fractions, which showcased the binding stoichiometry of 1 : 1, pointing towards the nature of chelates formed (Fig. S7). In the case of **CFN**, calcium ions showed best interaction with the nitrogen of the –CN group, oxygen of furan, and hydrogen of methyl group. The interaction is followed by fluorescence quenching due to the chelation-enhanced quenching (CHEQ) mechanism.[21]
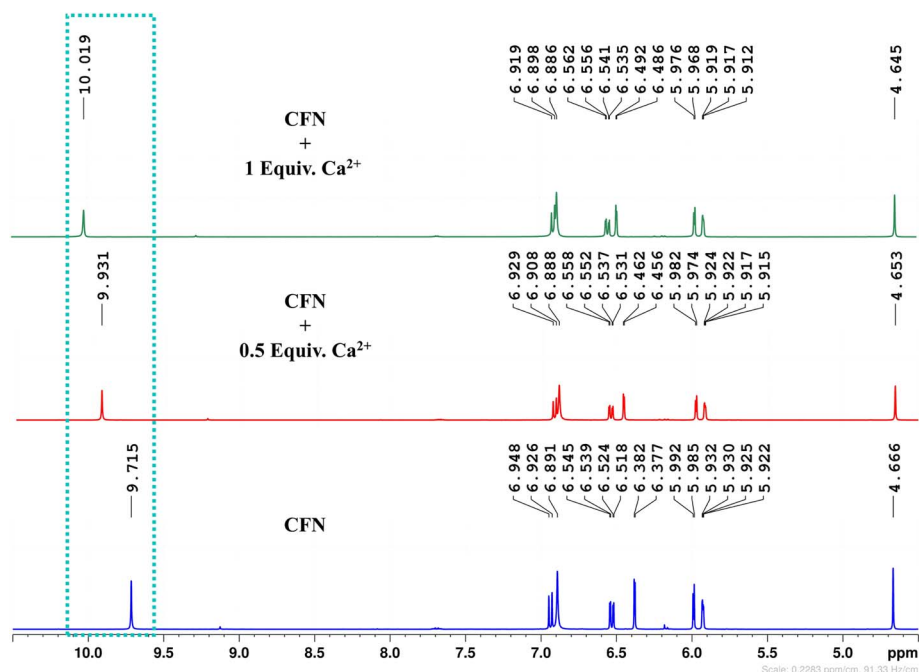

Fig. 8 ^{1}H NMR titration spectra of **CFN** upon the addition of 0.5 and 1.0 equivalents of calcium ions in DMSO-d_6.
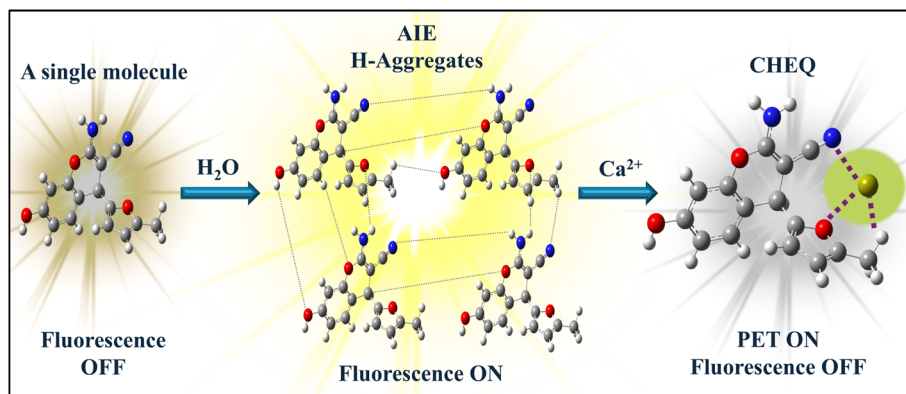
Fig. 9 Proposed sensing mechanism for calcium ion sensing by the **CFN** sensor.

^{1}H NMR titration was carried out to further validate the sensitive detection of Ca^{2+} *via* fluorescence quenching (S44–S46). The ^{1}H NMR assay was conducted before and after the titration with 0.5 and 1.0 equivalent of Ca^{2+} from CaCl$_2$ in DMSO-d$_6$. The NH$_2$ proton signals of **CFN** exhibited a significant downfield shift (Fig. 8), which suggests efficient complexation. The signal broadening is likely due to the paramagnetic nature of Ca^{2+}. The complexation of **CFN**@Ca^{2+} changes the overall electronic environment over the structure of **CFN**, which alters the proton NMR signals. Moreover, a significant change in the chemical shift of the –OH group in the structure of **CFN** was observed. This demonstrates that the complexation of **CFN**@Ca^{2+} induced ICT that reduces the charge density over the oxygen atom of the –OH group, which increases the acidity of this group. Due to this, the OH group of **CFN** easily deprotonates or starts to exchange its proton with the solvent, which is not only responsible for a downfield chemical shift, but also quenches the intensity of the signal. The proposed metal-sensor complexation mechanism is depicted in Fig. 9.

3.7.2 Optimization of geometry and thermodynamic stability. The geometry of the **CFN** molecule contains –OH, –CH$_3$, and –NH$_2$ as electron-donating functionalities and –CN as an electron-withdrawing group attached to the ring structures. It was crucial to depict the conformational studies along with the theoretical binding energy estimation of individual **CFN** molecules as well as the **CFN**–Ca^{2+} complex. The structural optimization of the **CFN** molecule and **CFN**–Ca^{2+} complex was executed on the wB97XD and B3LYP/6311G(d,p) basis sets by utilizing the Gaussian 09 program (Fig. S15). After structural optimization, binding energies at various interfaces between the **CFN** sensor and the Ca^{2+} ion were calculated to evaluate the most stable interaction site between **CFN** and Ca^{2+}. The basis set superposition error (BSSE) correction process was used to determine the binding energy of the **CFN**–Ca^{2+} complex. BSSE correction findings at various sites were 305.04, 205.01, and 263.07 kcal mol^{-1}, respectively. The most stable interaction site was site I, with a binding energy value of 305.04 kcal mol^{-1} selected for further DFT calculations (Fig. S16).

3.7.3 FMO and DOS studies. Significant tools like frontier molecular orbitals (FMO) and density of states (DOS) analysis are employed to interpret the stability and reactivity of substances. A piece of detailed and in-depth information regarding the sensitivity of the sensor towards the analyte will be attained by using their electronic properties. The attenuation of the HOMO–LUMO (H–L) gap of the sensor (H–L) signifies susceptibility, while the resistivity is the result of an increase in the H–L gap. Mainly, the reduction in HOMO–LUMO gap was observed due to intereaction between HOMO of **CFN** and LUMO of the analyte. The electronic properties of **CFN** were examined with and without Ca^{2+} ions. The interaction of **CFN** with Ca^{2+} ions showed a noteworthy reduction in the H–L energy gap and electron density. The H–L energy of the **CFN** sensor was at −5.76 eV and −0.81 eV, respectively. The H–L energy gap of the **CFN** sensor turned out to be 4.95 eV. Similarly, the H–L energy gap of the **CFN**–Ca^{2+} complex was reduced to 4.06 eV as its H–L energy levels were found to be at −7.03 eV and −2.97 eV, respectively (Fig. S17a).

The reduction in the H–L gape of the **CFN** sensor was observed due to the overlapping of molecular orbitals of **CFN** with the atomic orbital of Ca^{2+}. Moreover, the charge density distribution in the **CFN** sensor and its complex with Ca^{2+} was evaluated to identify the variation in their HOMO–LUMO energies. The H–L charge density was distributed over the sensor molecule before its interaction with the analyte. Nonetheless, the HOMO–LUMO charge density of the **CFN** sensor was slightly over Ca^{2+} ions after its interaction with the **CFN** sensor. Moreover, the entire characterization of the sensitivity/selectivity of **CFN** extensively depends on the DOS (density of state) analysis. DOS analysis was performed to evaluate the formation of new energy levels. The DOS results confirmed the formation of new energy levels (virtual energy states) and a sufficient reduction in the H–L gap in the **CFN** sensor–Ca^{2+} from 4.95 eV to 4.06 eV, which showed the significant sensitivity of **CFN** for Ca^{2+} ions, the eventual detection goal (Fig. S17b & c). DOS is one of the supreme DFT analyses to examine the sensitivity of the sensor.

3.7.4 EDD and NBO analysis. EDD and NBO analysis are also the two unconventional electron density transfer analyses that have been employed to further demonstrate the sensitivity of **CFN** against calcium ions. EDD provides a visual
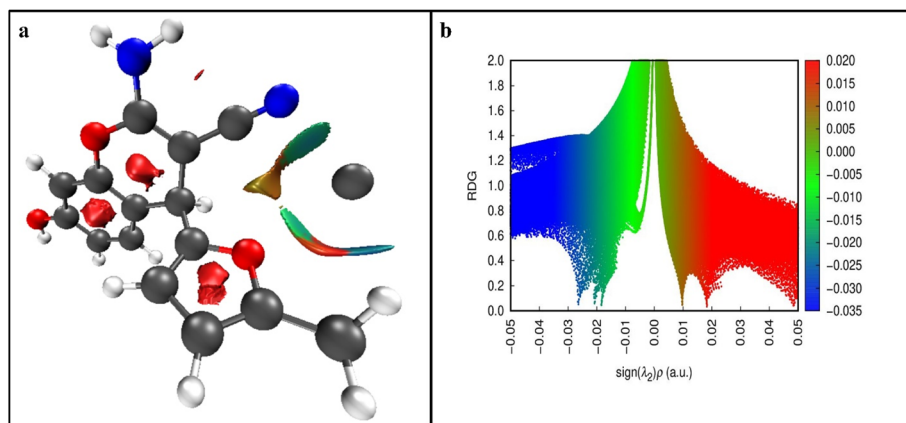
Fig. 10 (a) 3D NCI isosurface plot of the **CFN**–Ca^{2+} complex. (b) 2D RDG-NCI graph of the **CFN**–Ca^{2+} complex.

demonstration of charge transfer in the **CFN** and **CFN**–Ca^{2+} complex. As shown in Fig. S18, charge density reduction is demonstrated by the dark red and purple tones expounding the accumulation of charge density. The charge density accumulation between **CFN** and Ca^{2+} is evident from the purple color in the 3D EDD iso-surfaces of the **CFN**–Ca^{2+} complex. Similarly, the amount of electron density transfer from **CFN** to Ca^{2+} is calculated by NBO analysis. In NBO calculations, the quantity of charge represents the transfer of charge from the **CFN** sensor molecule to the electron-deficient Ca^{2+} ion. NBO represents the charge transfer from the **CFN** sensor (electron-rich) and Ca^{2+} ions (electron deficient). The **CFN** sensor expressed itself to have an NBO value of $-1.9119e^{-}$ upon **CFN**–Ca^{2+} complex formation.

3.7.5   NCI and QTAIM analysis. Three-dimensional NCI illustrates the nature of weak forces between **CFN** and Ca^{2+} ions. Three-dimensional NCI was deployed to make the iso-surface of the **CFN**–Ca^{2+} complex, in which the green contours are the representation of weak non-covalent interactions between **CFN** and Ca^{2+}, and red patches in the aromatic region of **CFN** depict the existence of repulsive forces (Fig. 10a). However, two-dimensional NCI studies were accomplished using the Multiwfn system. A spectral plot between ($\lambda 2\rho$) on the x-axis and reduced density gradient (RDG) on the y-axis was plotted in the result of 2D NCI. The existence of weak forces (van der Waals)

between **CFN** and Ca^{2+} ions is illustrated through green dotted lines, which were found in the region of -0.025 to -0.015 (Fig. 10b). However, red spikes revealed the existence of repulsive forces.

To further understand the weak interactions and to evaluate the BCPs (bond critical points) of bonds between **CFN** and Ca^{2+} ions, QTAIM studies were enacted using the Multiwfn program. Three bond critical points were obtained using QTAIM theoretical calculations (Fig. 11).

The presence of weak interactions (NCIs) between **CFN** and Ca^{2+} is represented through resulting parameter values such as $\nabla^2 \rho(r)$ and $\rho(r)$ in the range of 0.0149 to 0.0171 a. u. and 0.081 to 0.091 a. u. Correspondingly, and the other BCP values represent the parameters of NCIs given in Table S3.

4.   Analytical applications

4.1.   Determination of Ca^{2+} in human plasma

Accurate detection of Ca^{2+} levels in real samples is vital because of the crucial role of Ca^{2+} in various biological processes, highlighting the suggested sensor's effectiveness. Its cytotoxicity was evaluated to ensure that the **CFN** sensor is suitable for biological applications (Fig. S19). Human plasma (Ceruloplasmin, Human Plasma) samples were purchased from Sigma-Aldrich (Product No. 239799, Description: Ceruloplasmin, Human Plasma, CAS 9031-37-2, from human plasma, is involved in serum copper transport and plays a protective role against oxygen radicals generated by iron and ascorbate), and 30 μM of **CFN** was added to different amounts of human plasma in double-distilled water (0–50 μL mL^{-1}). The solution (DMF : H$_2$O, 1 : 9 v/v) was used to record the fluorescence spectra, as shown in Fig. S20a.

The results indicated a gradual decrease in fluorescence emission as a proportion of human plasma increased. Subsequently, different amounts of calcium were added to human plasma, and the resulting emission spectra were analyzed. The fluorescence emission spectra of **CFN** show a continuous decrease with the increase in Ca^{2+} concentration from 0 to 500 nM, as shown in Fig. S20b. Then 50 μL of human plasma was found to contain 300 nM of Ca^{2+}, calculated by comparing the
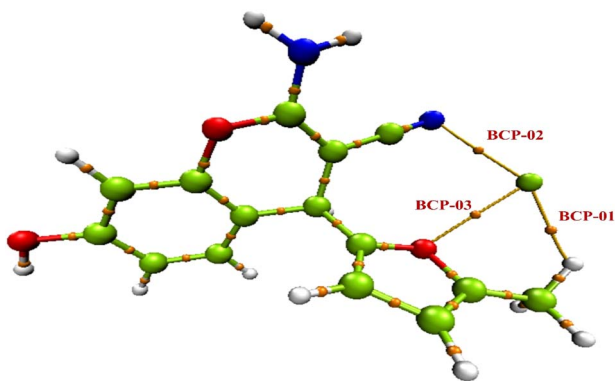

Fig. 11   QTAIM analysis results of the **CFN**–Ca^{2+} complex.
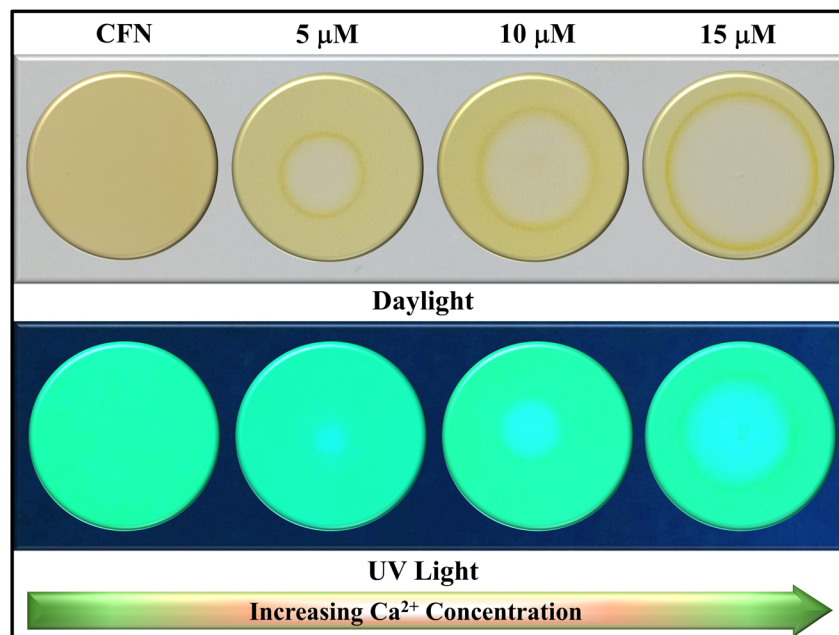
Fig. 12 CFN-coated handy TLC strips for the detection of Ca^{2+} in daylight and UV light.

change in emission spectra and plotting a standard linear graph before and after spiking with Ca^{2+}. The findings demonstrate the suitability of the **CFN** sensor for biological environments in quantifying Ca^{2+}.

4.2. Recovery experiments of water and milk samples

The real-time applicability of **CFN** for monitoring the calcium ion concentration in river water and tap water samples was investigated. Water samples from Kunhar River, Garhi Habibullah, normal tap water from COMSATS University Islamabad, Abbottabad Campus, and commercial tetra pack milk of Olpers Pakistan from Shaheen Chemists Abbottabad were collected in glass vials and were diluted to suitable concentrations in double-distilled water for further analysis, performed without any delay. After removing impurities with a 0.2 μm syringe filter, the samples were spiked with different amounts of Ca^{2+}. The fluorescence experiments were performed in triplicate with low to high spiking concentrations of 350 nM to 1000 nM. The graphs were plotted for all three types of samples (Fig. S21). Spike and recovery measurements were performed from the calibration curve of analyte concentration *versus* fluorescence results. The recovery percentages range from 102% to 109.8% with its relative standard deviation up to 2.37, showcasing the strong interaction of the sensor and the analyte (Tables S4–S6).

4.3. Portable handheld fluorescent films

Modernization with uncontrolled industrialization and mounting environmental pollution have created an urgent need for a straightforward, onsite monitoring mechanism for Ca^{2+} monitoring. Building on the promising sensing capabilities of **CFN**, we developed portable, reliable, and cost-effective sensor-loaded fluorescent films. A 30 μM solution in THF was prepared,

and thin-layer chromatography plates were dipped into the solution to fabricate these sensing films, which were dried at 35 °C for 20 minutes in a drying oven. The films appeared brownish in daylight while exhibiting a green color under 254 nm UV light (Fig. 12).

When 10 μM Ca^{2+} was applied to these active fluorescent films, changes in color and absorption were observed as brown turns to greyish shade under daylight and light green turning to light blue under UV, respectively (Fig. 12). The results confirmed the effectiveness of the sensor-coated TLC films against the Ca^{2+} analyte as a convenient, efficient, potable and straightforward solution for onsite monitoring.

4.4. Fabrication of logic devices

Digital computing has modernized and simplified fluorescence sensing by converting fluorescence emission signals into chemically encoded information through the use of logic
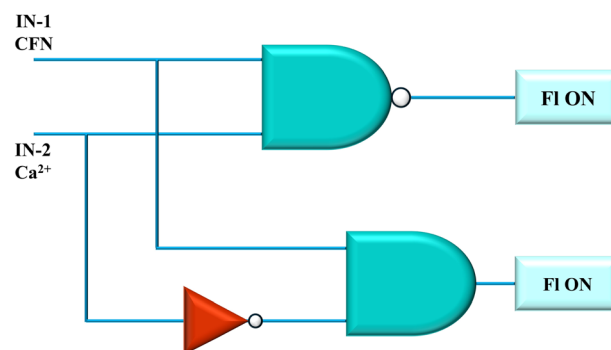

Fig. 13 Logic gate flow sheet configuration of **CFN** for calcium ion sensing.

gates.[73] Combining innovation and encouraging **CFN** sensor spectroscopic results, we developed a logic gate framework. A logic circuit consisting of NAND, AND, and NOT gates is used in the suggested configuration. Input-1 (IN-1) and input-2 (IN-2) are the corresponding input signals from **CFN** and Ca^{2+}. Fig. 13 shows an employed setup consisting of an output signal (OUT) at an emission spectrum of 444 nm.

The threshold for the detection of Ca^{2+} was set by the emission peak at 420 nm. The signals at 420 nm wavelength or higher were categorized as "ON" or "1", while those below this were marked as "OFF" or "0". Therefore, the logic gate demonstrated "OFF" when the complex **CFN**–Ca^{2+} was supplied as input and reverted to "ON" when only **CFN** was the input because of the use of a NAND gate. A truth table based on the logic circuit results that corresponded to fluorescent emission was drawn (Table S7). In conclusion, our research indicates that these sensors could be effectively integrated into contemporary electronic devices, facilitating easier and more efficient analytical procedures.

5. Conclusion

In conclusion, a novel chromene-based AIE-active and solvatochromic **CFN** sensor was synthesized and characterized by NMR spectroscopy. The **CFN** sensor with novel structural features and structure–property relationship demonstrated solvatochromism, large Stokes shift (120 nm), and aggregation-induced emission enhancement (AIE). The **CFN** sensor was employed for highly specific and sensitive colorimetric sensing of Ca^{2+} in an aqueous solution (λ_{em} = 444 nm, DMF : H_2O, 1 : 9 v/v) in the presence of potential interferents. Chelation-enhanced fluorescence quenching (CHEQ) is involved as a primary sensing mechanism in the sensing of Ca^{2+} ions. The **CFN**@Ca^{2+} complexation was confirmed through titration NMR analysis, dynamic light scattering (DLS) analysis, and DFT studies. A continuous variation method confirmed 1 : 1 binding stoichiometry between the **CFN** and Ca^{2+} ion. Moreover, the detection and quantification limit were found to be 10.5 nM and 35 nM, respectively. Furthermore, the **CFN** sensor was employed for the quantification of Ca^{2+} ions in real samples, including human plasma, river water, tap water and commercial milk using spike recovery measurements. Additionally, a portable, cost-effective fluorescent TLC strip was fabricated for effective on-site monitoring of Ca^{2+} ions. Finally, a logic gate was constructed for the electronic monitoring of Ca^{2+} ions.

Conflicts of interest

The authors declare that they have no known competing financial interests or personal relationships that could have appeared to influence the work reported in this paper.

Data availability

The scientific data supporting this article have been included as part of the supplementary information (SI). Supplementary information: absorption and emission spectra, DLS analysis, theoretical studies and NMR spectra. See DOI: **https://doi.org/10.1039/d5ra06005b**.

References

1 L. Li, X. Ma, W. Dong, P. Miao and Y. Tang, *Bioconjugate Chem.*, 2018, **29**, 1021–1024.

2 M. W. Berchtold, H. Brinkmeier and M. Muntener, *Physiol. Rev.*, 2000, **80**, 1215–1265.

3 J. Zheng, X. Zeng and S. Wang, *Sci. China Life Sci.*, 2015, **58**, 1–5.

4 J. Pepe, L. Colangelo, F. Biamonte, C. Sonato, V. C. Danese, V. Cecchetti, M. Occhiuto, V. Piazzolla, V. De Martino and F. Ferrone, *Endocrine*, 2020, **69**, 485–495.

5 G. Zündorf and G. Reiser, *Antioxid. Redox Signaling*, 2011, **14**, 1275–1288.

6 M. Salek-Maghsoodi, Z. Golsanamlu, S. Sadeghi-Mohammadi, M. Gazizadeh, J. Soleymani and R. Safaralizadeh, *RSC Adv.*, 2022, **12**, 31535–31545.

7 M. P. Mattson, *Aging Cell*, 2007, **6**, 337–350.

8 S. Takano, H. Kaji, F. Hayashi, K. Higashiguchi, S. Joukei, Y. Kido, J. Takahashi and K. Osawa, *Anal. Chem. Insights*, 2012, **7**, ACI.S9681.

9 A. B. Borle and F. N. Briggs, *Anal. Chem.*, 1968, **40**, 339–344.

10 H. Vaessen and C. G. van de Kamp, *Z. Lebensm. Unters. Forsch.*, 1990, **190**, 199–204.

11 K. P. Jochum, D. Scholz, B. Stoll, U. Weis, S. A. Wilson, Q. Yang, A. Schwalb, N. Börner, D. E. Jacob and M. O. Andreae, *Chem. Geol.*, 2012, **318**, 31–44.

12 H. Kaila, M. Ambasana, R. Thakkar, H. Saravaia and A. Shah, *Indian J. Pharmaceut. Sci.*, 2010, **72**, 592.

13 W. Zhang, H. Zhang and A. Zhou, *Microchem. J.*, 2019, **147**, 215–223.

14 S. Erdemir, O. Kocyigit and S. Malkondu, *J. Photochem. Photobiol., A*, 2022, **425**, 113713.

15 Y. Wu, Y. Zhang, Z. Xu, X. Guo, W. Yang, X. Zhang, Y. Liao, M. Fan and D. Zhang, *Biosensors*, 2022, **12**, 917.

16 X. Li, C. Pan, J. Cao, Z. Liu, Z. Zhu, C. Yan, W. Zhao, W.-H. Zhu and Q. Wang, *Biomaterials*, 2022, **289**, 121778.

17 K. Khurshid, S. Saeed, M. A. Assiri, A. Shabbir and S. A. Shahzad, *Spectrochim. Acta, Part A*, 2025, 126421.

18 J. Yang, M. Fang and Z. Li, *Aggregate*, 2020, **1**, 6–18.

19 J. Luo, Z. Xie, J. W. Y. Lam, L. Cheng, H. Chen, C. Qiu, H. S. Kwok, X. Zhan, Y. Liu, D. Zhu and B. Z. Tang, *Chem. Commun.*, 2001, 1740–1741, DOI: **10.1039/B105159H**.

20 Muqadas, A. Shabbir, M. A. Assiri, M. Khan and S. A. Shahzad, *J. Mol. Liq.*, 2025, **427**, 127399.

21 Muqadas, A. Shabbir, M. Khan, M. A. Assiri, A. M. Khan and S. A. Shahzad, *Microchem. J.*, 2025, **214**, 114129.

22 Y. Yang, D. Deng, X. Deng, Z. Chen and S. Pu, *Molecules*, 2022, **27**, 4740.

23 C. Zhu, R. T. K. Kwok, J. W. Y. Lam and B. Z. Tang, *ACS Appl. Bio Mater.*, 2018, **1**, 1768–1786.

24 J. Heo, D. P. Murale, H. Y. Yoon, V. Arun, S. Choi, E. Kim, J. S. Lee and S. Kim, *Aggregate*, 2022, **3**, e159.

25 C. Wu, M. DeLong, Z. Vardeny and J. Ferraris, *Synth. Met.*, 2003, **137**, 939–941.

26 R. Kabe, H. Nakanotani, T. Sakanoue, M. Yahiro and C. Adachi, *Adv. Mater.*, 2009, **21**, 4034–4038.

27 J. Gierschner, L. Lüer, B. Milián-Medina, D. Oelkrug and H.-J. Egelhaaf, *J. Phys. Chem. Lett.*, 2013, **4**, 2686–2697.

28 F. C. Spano, *Accounts Chem. Res.*, 2010, **43**, 429–439.

29 S. Basak, N. Nandi, K. Bhattacharyya, A. Datta and A. Banerjee, *Phys. Chem. Chem. Phys.*, 2015, **17**, 30398–30403.

30 N. Ryu, Y. Okazaki, E. Pouget, M. Takafuji, S. Nagaoka, H. Ihara and R. Oda, *Chem. Commun.*, 2017, **53**, 8870–8873.

31 M. Kasha, *Radiat. Res.*, 2012, **178**, AV27–AV34.

32 J. Modi, S. Patel, G. K. Mahato, B. Mahto and G. Chandra, *ChemPhotoChem*, 2024, **8**, e202300284.

33 S. M. Radiul, J. Chowdhury and S. Hazarika, *J. Mol. Struct.*, 2023, **1275**, 134606.

34 V. Martínez Martínez, F. López Arbeloa, J. Bañuelos Prieto and I. López Arbeloa, *J. Phys. Chem. B*, 2005, **109**, 7443–7450.

35 S. De, S. Das and A. Girigoswami, *Spectrochim. Acta, Part A*, 2005, **61**, 1821–1833.

36 N. H. Mudliar and P. K. Singh, *Chem.–Eur. J.*, 2016, **22**, 7394–7398.

37 M. Cigan, J. Donovalová, V. Szöcs, J. Gaspar, K. Jakusová and A. Gaplovsky, *J. Phys. Chem.*, 2013, **117**, 4870–4883.

38 S. Chakraborty, P. Debnath, D. Dey, D. Bhattacharjee and S. A. Hussain, *J. Photochem. Photobiol., A*, 2014, **293**, 57–64.

39 A. K. Chibisov, G. V. Zakharova and H. Görner, *Phys. Chem. Chem. Phys.*, 1999, **1**, 1455–1460.

40 A. K. Chibisov, G. V. Zakharova and H. Görner, *Phys. Chem. Chem. Phys.*, 2001, **3**, 44–49.

41 C. Peyratout and L. Daehne, *Phys. Chem. Chem. Phys.*, 2002, **4**, 3032–3039.

42 U. Rösch, S. Yao, R. Wortmann and F. Würthner, *Angew. Chem.*, 2006, **118**, 7184–7188.

43 K. Khurshid, S. A. Shahzad, M. A. Assiri, A. Shabbir, T. Javid and H. Irshad, *RSC Adv.*, 2024, **14**, 21682–21691.

44 A. Shabbir, S. A. Shahzad, A. Y. A. Alzahrani, Z. A. Khan, M. Yar and W. Rauf, *Spectrochim. Acta, Part A*, 2025, **327**, 125414.

45 A. Shabbir, M. M. Iqbal, M. A. Assiri, T. Javid, A. Pervaiz, A. H. Khan, A. Hassan and S. A. Shahzad, *Spectrochim. Acta, Part A*, 2025, **333**, 125895.

46 A. Majeed, S. A. Shahzad, M. A. Assiri, K. O. Khan, H. Rabale and A. Shabbir, *Spectrochim. Acta, Part A*, 2025, 125802.

47 M. J. Frisch, *et al.*, *Gaussian 09; Revision D.01*, Gaussian, Inc., Wallingford, CT, 2013.

48 Muqadas, A. Shabbir, M. A. Assiri, M. Khan and S. A. Shahzad, *J. Mol. Liq.*, 2025, **427**, 127399.

49 M. Khalid, A. Ali, S. Asim, M. N. Tahir, M. U. Khan, L. C. C. Vieira, A. F. de la Torre and M. Usman, *J. Phys. Chem. Solids*, 2021, **148**, 109679.

50 R. Dennington, T. Keith and J. Millam, *KS: Dennington*, Semichem Inc., Shawnee Mission, 2009.

51 W. Humphrey, A. Dalke and K. Schulten, *J. Mol. Graph.*, 1996, **14**, 33–38.

52 B. Mennucci, *Wiley Interdiscip. Rev.: Comput. Mol. Sci.*, 2012, **2**, 386–404.

53 C. F. Matta and R. J. Boyd, *An Introduction to the Quantum Theory of Atoms in Molecules*, 2007, **1**, 1–34.

54 S. R. Ankireddy and J. Kim, *Sens. Actuators, B*, 2018, **255**, 3425–3433.

55 S. T. Hong, M. S. Kim, B. R. Kim, E. J. Lee, Y. U. Yoon, K. C. Paik, M. S. Han, E. S. Kim and B. R. Cho, *Talanta*, 2022, **244**, 123408.

56 Y. Shen, S. Zhou, W. He, J. Gao, Y. Yang, K. Xiao and Z. Yao, *J. Photochem. Photobiol., A*, 2023, **442**, 114771.

57 H. Zhang, C. Yin, T. Liu, Y. Zhang and F. Huo, *Spectrochim. Acta, Part A*, 2017, **180**, 211–216.

58 L. J. Gomes, M. Outis, C. S. Gomes, A. C. Tomé and A. J. Moro, *Molecules*, 2024, **29**, 527.

59 L. Cao, C. Jia, Y. Huang, Q. Zhang, N. Wang, Y. Xue and D. Du, *Tetrahedron Lett.*, 2014, **55**, 4062–4066.

60 S. Kacmaz, K. Ertekin, O. Oter, D. Mercan, E. Cetinkaya and E. Celik, *J. Lumin.*, 2014, **147**, 265–272.

61 A. S. Tanwar, S. Hussain, A. H. Malik, M. A. Afroz and P. K. Iyer, *ACS Sens.*, 2016, **1**, 1070–1077.

62 M. Haidekker, T. Brady, D. Lichlyter and E. Theodorakis, *Bioorg. Chem.*, 2005, **33**, 415–425.

63 J. Palion-Gazda, B. Machura, T. Klemens, A. Szlapa-Kula, S. Krompiec, M. Siwy, H. Janeczek, E. Schab-Balcerzak, J. Grzelak and S. Maćkowski, *Dyes Pigm.*, 2019, **166**, 283–300.

64 W. Liu, Y. Wang, J. Yang, X. Li, X. Wang and L. Ma, *Dyes Pigm.*, 2020, **175**, 108149.

65 F. Han, L. Chi, W. Wu, X. Liang, M. Fu and J. Zhao, *J. Photochem. Photobiol., A*, 2008, **196**, 10–23.

66 S. Saeed, K. Khurshid, M. A. Assiri, A. Shabbir and S. A. Shahzad, *Dyes Pigm.*, 2025, **239**, 112813.

67 H. Auweter, H. Haberkorn, W. Heckmann, D. Horn, E. Lüddecke, J. Rieger and H. Weiss, *Angew. Chem., Int. Ed.*, 1999, **38**, 2188–2191.

68 H. Wu, L. Xue, Y. Shi, Y. Chen and X. Li, *Langmuir*, 2011, **27**, 3074–3082.

69 M. Yang, D. Xu, W. Xi, L. Wang, J. Zheng, J. Huang, J. Zhang, H. Zhou, J. Wu and Y. Tian, *J. Org. Chem.*, 2013, **78**, 10344–10359.

70 M. A. Haidekker and E. A. Theodorakis, *Org. Biomol. Chem.*, 2007, **5**, 1669–1678.

71 P. E. Johnson, H. C. Lukaski and T. D. Bowman, *J. Nutr.*, 1987, **117**, 501–507.

72 L. Konečný, Z. Lomozová, G. Karabanovich, J. Roh, K. Vávrová and P. Mladěnka, *J. Biol. Inorg. Chem.*, 2024, 1–16.

73 A. P. de Silva and N. D. McClenaghan, *Chem.–Eur. J.*, 2004, **10**, 574–586.